

Experimental evidence for collisional shock formation via two obliquely merging supersonic plasma jets

Elizabeth C. Merritt,^{1,2, a)} Auna L. Moser,¹ Scott C. Hsu,^{1, b)} Colin S. Adams,^{1,2} John P. Dunn,¹ A. Miguel Holgado,¹ and Mark A. Gilmore²

¹⁾ Los Alamos National Laboratory, Los Alamos, NM, 87545, USA

²⁾ University of New Mexico, Albuquerque, NM, 87131, USA

(Dated: 15 February 2019)

We report spatially resolved measurements of the oblique merging of two supersonic laboratory plasma jets. The jets are formed and launched by pulsed-power-driven railguns using injected argon, and have electron density $\sim 10^{14} \text{ cm}^{-3}$, electron temperature $\approx 1.4 \text{ eV}$, ionization fraction near unity, and velocity $\approx 40 \text{ km/s}$ just prior to merging. The jet merging produces a few-cm-thick stagnation layer, as observed in both fast-framing camera images and multi-chord interferometer data, consistent with collisional shock formation [E. C. Merritt et al., Phys. Rev. Lett. **111**, 085003 (2013)].

I. INTRODUCTION

We have conducted experiments on the oblique merging of two supersonic plasma jets¹ on the Plasma Liner Experiment² (PLX) at Los Alamos National Laboratory. These experiments were the second in a series of experiments intended to demonstrate the formation of imploding spherical plasma liners via an array of merging supersonic plasma jets.^{3–5} The latter has been proposed^{3,6,7} as a standoff compression driver for magneto-inertial fusion^{8–10} (MIF) and, in the case of targetless implosions, for generating cm-, μs -, and Mbar-scale plasmas for high-energy-density physics¹¹ research. In our first set of experiments, the parameters and evolution of a single propagating plasma jet were characterized in detail.² The next step beyond this work, a thirty-jet experiment to form and assess spherically imploding plasma liners, has been designed^{3,5,12} but not yet fielded. A related jet-merging study^{13–15} was also conducted recently by HyperV Technologies.

The supersonic jet-merging experiments reported here are also relevant to the basic study of plasma shocks¹⁶ in a semi- to fully collisional regime. Related studies include counter-streaming laser-produced plasmas supporting hohlraum design for indirect-drive inertial confinement fusion^{17–19} and for studying astrophysically relevant shocks,^{20–24} colliding plasmas using wire-array Z pinches,^{25,26} and applications such as pulsed laser deposition²⁷ and laser-induced breakdown spectroscopy.²⁸ Primary issues of interest in these studies include the identification of shock formation, the formation of a stagnation layer^{29–31} between colliding plasmas, and the possible role of two-fluid and kinetic effects on plasma interpenetration.^{32–35}

In this paper we present detailed measurements of the stagnation layer that forms between two obliquely merging supersonic plasma jets in a semi- to fully collisional

regime. First, we briefly describe the experimental setup (Sec. II). Then we discuss observations of the stagnation layer emission morphology (Sec. III) and density enhancements (Sec. IV). We also examine the observed stagnation layer thickness in the context of various estimated collision length scales and two-fluid plasma shock theory (Sec. V). Collectively, our observations are shown to be consistent with collisional shocks. We close with a discussion of the implications of our results on proposed imploding plasma liner formation experiments (Sec. VI) and a summary (Sec. VII).

II. EXPERIMENTAL SETUP

Two plasma railguns are mounted on adjacent ports of a 2.7-m-diameter spherical vacuum chamber [Fig. 1(a)], with a half-angle $\approx 12^\circ$ between the jet axes of propagation and a distance $\approx 46 \text{ cm}$ between the gun nozzles. At the nozzle exit, individual jets have initial parameters of peak electron density $n_e \approx 2 \times 10^{16} \text{ cm}^{-3}$, peak electron temperature $T_e \approx 1.4 \text{ eV}$, diameter = 5 cm, and axial length $\approx 20 \text{ cm}$.² In this series of experiments, the initial jet velocity $V_{\text{jet}} \approx 40 \text{ km/s}$ and Mach number $M \equiv V_{\text{jet}}/C_{s,\text{jet}} > 10$, where $C_{s,\text{jet}}$ is the sound speed in the jet. More details on the railguns and the characterization of single-jet propagation are reported elsewhere.² The jets are individually very highly collisional (thermal mean free paths $\lambda_i \approx \lambda_e \sim 1 \mu\text{m}$ in a $\sim 10\text{-cm}$ -scale plasma), but the characteristic interaction length ($\sim 1 \text{ cm}$, details given in Sec. V) between counter-propagating jet ions is on the order of the thickness of the observed stagnation layer that forms between the obliquely merging jets.

The key diagnostics for our merging experiments are a visible-to-near-infrared survey spectrometer (0.275 m focal length with 600 lines/mm grating and $0.45 \mu\text{s}$ gating on the 1024-pixel microchannel plate array detector), an eight-chord 561 nm laser interferometer,^{36,37} and an intensified charged-coupled-device (CCD) visible-imaging camera (DiCam Pro, 1280×1024 pixels, 12-bit dynamic range). The CCD camera field-of-view extends from

^{a)} Electronic mail: emerritt@lanl.gov

^{b)} Electronic mail: scotthsu@lanl.gov

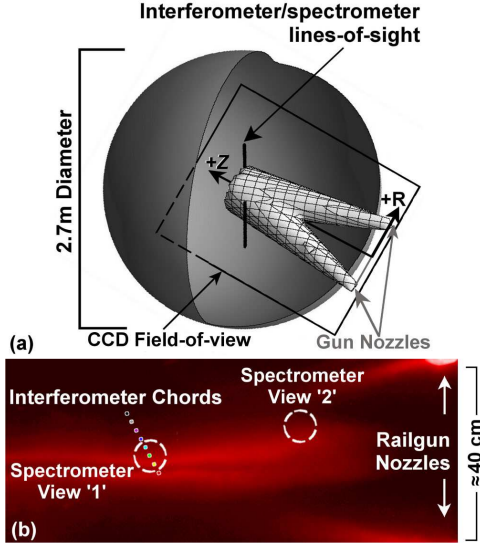


FIG. 1. (a) Schematic showing the spherical vacuum chamber, two merging plasma jets, (R, Z) coordinates used in the paper, approximate interferometer (representing all 8 chords) and spectrometer (view ‘1’) lines-of-sight, and CCD camera field-of-view. (b) Location of interferometer chords (dots, $Z \approx 85$ cm, inter-chord spacing = 1.5 cm), and spectroscopy views (dashed circle, diameter ≈ 7 cm) overlaid on a cropped CCD image of jet merging. Spectroscopy views ‘1’ and ‘2’ are located at $(R, Z) \approx (3.75$ cm, 85 cm) and (12 cm, 55 cm), respectively.

$Z \approx 0$ –156 cm. The interferometer chords and spectrometer view ‘1’ intersect the stagnation layer at $Z \approx 85$ cm [Fig. 1(b)], with an angle of $\approx 36^\circ$ with respect to the jet-merging plane (into the page). The line formed by the interferometer chords is roughly transverse to the stagnation layer ($\approx 30^\circ$ with respect to the R direction), with inter-chord spacing of ≈ 1.5 cm, spanning $R \approx 0.75$ –11.25 cm. The $\approx 30^\circ$ angle with respect to R introduces slight temporal offsets ($\approx 0.2 \mu\text{s}$ between adjacent interferometer chords) for interferometer data plots versus R . The $\approx 36^\circ$ angle between the chords and the merge plane may lead to underestimates of plasma density enhancements and overestimates of local density minima due to the chords intersecting both shocked and unshocked plasma regions. Spectrometer view ‘1’ is centered on the interferometer chord at $(R, Z) = (3.75$ cm, 85 cm). Spectrometer view ‘2’ is located at $(R, Z) \approx (12$ cm, 55 cm) and is oriented $\approx 31^\circ$ relative to the merge plane. The collimated spectrometer field-of-view has a divergence of 2.4° and a diameter $\approx 7 \pm 0.5$ cm at the measurement position. Plasma jet velocity is determined via an array of intensified photodiode detectors.² Figure 2 shows a sequence of twelve CCD camera images (a different shot for each time; images are very reproducible) of the time evolution of jet merging and the formation of a stagnation layer along the jet-merging plane (midplane, horizontal in the images), with a double-peaked emission

profile transverse (R direction, vertical in the images) to the layer. Experiments were conducted with top jet only, bottom jet only, and both jets firing to enable the most direct comparison between single- and merged-jet measurements.

We have measured the jet magnetic field strength (transverse to the jet propagation direction) using magnetic probes mounted at two locations along the exterior of the cylindrical railgun nozzle. The probe coils have nominal turns \times area of 10 cm^2 (at the relevant frequency of 50 kHz, corresponding to the frequency of the gun current that produces the jet magnetic field), and the signals are passively integrated with a time constant of 0.322 ms. The jet is maintained at a constant diameter of 5 cm inside the nozzle. The field strength decreases from ≈ 0.14 T at $Z = -16$ cm to ≈ 0.075 T near the nozzle exit ($Z = 0$ cm), with a decay time of $5.6 \mu\text{s}$ (see Fig. 3). Extrapolating the decay to $t = 24 \mu\text{s}$ (i.e., $\approx 12 \mu\text{s}$ after the jet exits the nozzle), the field would be approximately 0.01 T. Based on the parameters at initial jet merging ($n_e = 2 \times 10^{14} \text{ cm}^{-3}$, $T_e = 1.4 \text{ eV}$,² $B = 0.01$ T and $v = 40$ km/s), then the ratio of the jet kinetic energy density ($\rho v^2/2$) to the magnetic energy density ($B^2/2\mu_0$) is 270. The corresponding magnetic Reynold’s number $R_m \approx 1.4$ (using a jet radial length scale of 5 cm for diffusion and a propagation distance 40 cm for advection), consistent with strong resistive field decay. If instead of being spatially uniform, the axial current producing the measured transverse magnetic field is peaked and mostly contained within a radius $r_0 < r_{\text{nozzle}} = 2.5$ cm, then the peak field inside the jet would be larger than the measured value by a factor $B_0 r_{\text{nozzle}}/r_0$, where $B_0 = 0.0035$ T. If $r_0 = 1$ cm, then the peak $B = 0.35$ T, which, extrapolating to $t = 24 \mu\text{s}$, would give a kinetic-to-magnetic energy density ratio of ≈ 47 , still much larger than unity. We also point out that the inferred decay time of $5.6 \mu\text{s}$ ignores jet expansion and cooling, meaning that $5.6 \mu\text{s}$ is an upper bound. Thus, we ignore magnetic field effects in this paper. These magnetic field measurements were taken during hydrogen experiments (the rest of the paper reports argon results), but $T_e \approx 1.4$ eV, and thus the magnetic diffusivity, were similar in both cases.

The argon plasma jets in these experiments likely had high levels of impurities. The post-shot chamber pressure rise for gas-injection-only was about 30% of that of a full railgun discharge, implying possible plasma impurity levels of up to 70%. Identification of bright aluminum and oxygen spectral lines in our data¹ suggests that impurities are from the zirconium-toughened-alumina (0.15 ZrO_2 and 0.85 Al_2O_3) railgun insulators. Because the exact impurity fractions as a function of space and time in our jets are unknown, we bound our analysis by considering the two extreme cases of (i) 100% argon and (ii) 30% argon with 70% impurities. For case (ii), we approximate the jet composition as 43% oxygen and 24% aluminum (based on their ratio in zirconium-toughened-alumina) for spectroscopy analysis.

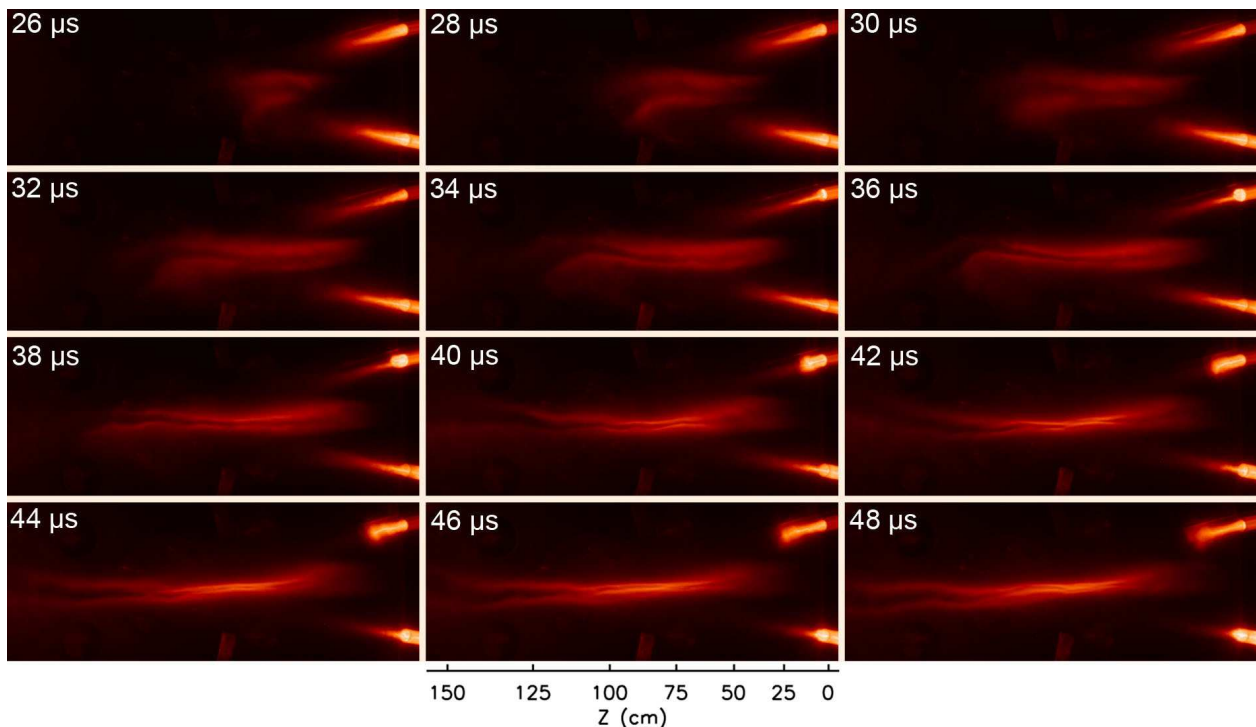


FIG. 2. False-color, cropped CCD images (log intensity, 20 ns exposure) of oblique jet merging [shots 1130, 1129, 1128, 1127, 1125, 1122, 1120, 1132, 1134, 1136, 1138, 1140 (in order of timing)]. In each image, the two railgun nozzles (≈ 46 cm apart) are visible on the right-hand-side, and the stagnation layer is oriented horizontally. All images have the same scale, which has a slightly nonlinear pixel-to-cm conversion due to the camera angle and optics.

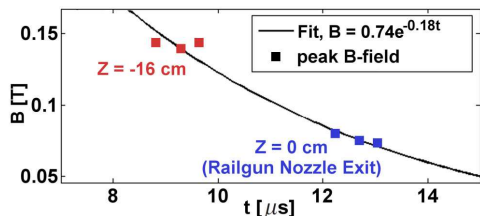


FIG. 3. Peak magnetic field (transverse to rails and jet propagation direction) vs. time (shots 2444, 2445, 2446, 2448, 2449, 2450). The data (squares) are from magnetic probes mounted at two positions along the exterior of the cylindrical railgun nozzle.

III. CONSISTENCY OF STAGNATION LAYER MORPHOLOGY WITH HYDRODYNAMIC SHOCKS

A. Oblique shock morphology

Because inherently two-dimensional (2D) effects, such as non-uniform jet profiles, and time-dependent effects do not permit a tractable analytic treatment of our problem and require full 2D simulations, we use analytic 1D hydrodynamic theory to gain qualitative insight into the shock boundary morphology. The assumption of parallel, uniform flow within each jet [see Fig. 4(a)] reduces

this to a 1D problem analogous to supersonic flow past a wedge or compression corner.^{38,39} Comparing with the 1D theory, we show that the observed emission layers (Fig. 2) are consistent with post-shocked plasma,¹ with their edges (at larger $|R|$) corresponding to the shock boundaries.

Figure 4(a) shows a simple schematic of the jet interaction, where δ is the angle between the jet flow direction and the midplane, M_1 is the initial (pre-interaction) Mach number, and $\beta \equiv \beta(\delta, M_1)$ is the angle between the jet-flow direction and the position of an oblique shock boundary.^{11,39} Figure 4(b) shows a similar structure in a merged-jet CCD image. In this system, the turning angle $\delta \equiv \delta(Z_i)$ is given by $\tan \delta = (23 \text{ cm})/Z_i$, where Z_i is the point at which the jets first interact, as determined by the appearance of emission [as indicated in Figs. 4(b) and 4(c)]. The shock boundary angle β is given by³⁸

$$\frac{23 \text{ cm}}{Z_i} = 2 \cot \beta \left[\frac{M_1^2 \sin^2 \beta - 1}{M_1^2 (\gamma + \cos 2\beta) + 2} \right], \quad (1)$$

and the opening angle of the shock relative to the midplane is $\beta - \delta$. Determination of Z_i from plasma emission may slightly overestimate Z_i , but the errors introduced are small compared to the actual difference between predicted and observed values of $\beta - \delta$ (presented below). Also, a slight overestimate of Z_i does not affect the discussion in Sec. III B regarding a possible shock transition.

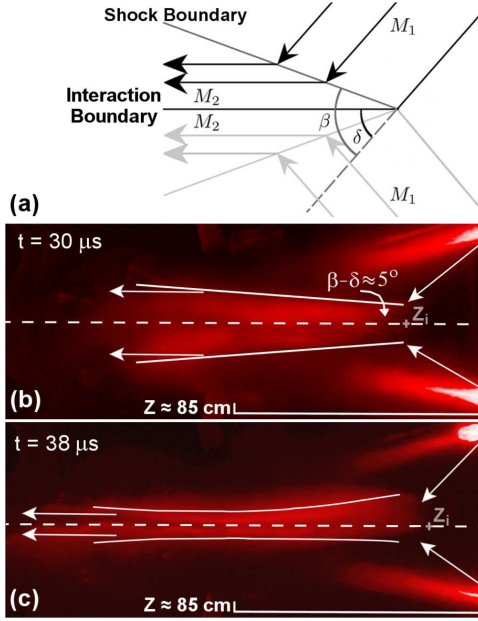


FIG. 4. (a) Simple schematic of the interaction of two obliquely interacting supersonic flows with initial Mach numbers M_1 . Flows are incident on the midplane with angle δ . A shock boundary forms at angle β with respect to the original flow direction. Post-shock flows have Mach number M_2 and flow direction parallel to the midplane. (b) CCD image with postulated shock boundaries (solid white lines) and initial jet interaction distances Z_i for shot 1128 at $t = 30 \mu\text{s}$ ($Z_i \approx 30 \text{ cm}$) and (c) shot 1120 at $t = 38 \mu\text{s}$ ($Z_i \approx 21 \text{ cm}$). The field-of-view is the same for both CCD images.

Assuming $T_e = 1.4 \text{ eV}$, mean charge $\bar{Z} = 0.94$ (both inferred from spectroscopy at $Z = 41 \text{ cm}$),² and specific heat ratio $\gamma = 1.4$,¹² then a 100% argon plasma jet with $V_{\text{jet}} = 40 \text{ km/s}$ has $M = 19$. For the 30%/70% mixture composition, $T_e = 1.4 \text{ eV}$ and $\bar{Z} = 0.92$ (see Sec. IV), which are similar to the 100% argon case. To place a stringent lower bound on M for the 30%/70% case, we use an ion-to-proton mass ratio $\mu = \mu_O = 16$ because oxygen is the lightest element in the impurity mixture. Thus, we estimate that $12 < M < 19$. We find that predicted $\beta - \delta$ values are very similar for $M = 12$ and $M = 19$ for a range of Z [Fig. 5(a)].

We observe that Z_i falls from $Z_i \approx 45 \text{ cm}$ at $t = 26 \mu\text{s}$ to $Z_i \approx 18 \text{ cm}$ at $t = 36 \mu\text{s}$ [Fig. 5(b)], consistent with jet axial expansion² that reduces the velocity and thus increases the jet expansion angle for the rear portion of the jet. A second dip in Z_i beginning at $t \approx 47 \mu\text{s}$ is due to the arrival of a trailing jet (created by ringing in the underdamped railgun current²) at the merge region. For early times $t \approx 24\text{--}33 \mu\text{s}$ ($Z_i \approx 45\text{--}25 \text{ cm}$), the 1D theory predicts oblique shock formation consistent with the observed wedge-shaped emission boundary, as illustrated in Fig. 4(b). In this case, the measured $\beta - \delta \approx 5^\circ$. For $M = 12\text{--}19$, the theoretically predicted $\beta - \delta \approx 11^\circ$, which is within approximately a factor of two of the ex-

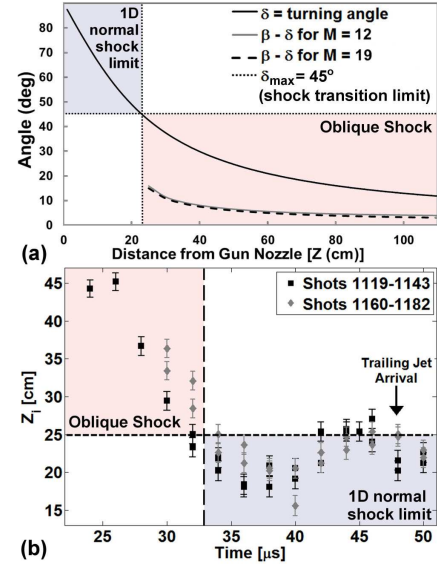


FIG. 5. (a) Plot of δ and $\beta - \delta$ vs. Z for both $M = 12$ and $M = 19$ (from 1D hydrodynamic theory). The predicted threshold turning angle (also from the 1D theory), $\delta = \delta_{\text{max}} = 45^\circ$, and corresponding $Z_i(\delta_{\text{max}}) \approx 25 \text{ cm}$ are marked with horizontal and vertical dotted lines, respectively. (b) Plot of Z_i vs. time for shots 1119–1143 and shots 1160–1182. Error bars correspond to a ± 7.5 pixel offset along the Z axis during image processing. The 1D theoretical cutoff for oblique shock formation, $Z_i \approx 25 \text{ cm}$, is indicated by a horizontal dashed line.

perimentally inferred value. This is reasonable agreement given that the 1D prediction does not include 2D/3D nor plasma equation-of-state¹⁴ (EOS) effects.

B. Speculation on shock transition

There is a possible emission morphology transition between earlier and later times [i.e., Fig. 4(b) versus 4(c)]. For the theoretical 1D problem with uniform, parallel flow [with an angle δ relative to the “interaction boundary” in Fig. 4(a)], there is a threshold $\delta_{\text{max}} \approx 45^\circ$ ($Z_i \approx 25 \text{ cm}$) beyond which no oblique shock forms. In 2D theory, this corresponds to a detached shock, which we treat in the 1D analysis by considering the limiting case of a normal shock. Predicting the exact structure of a detached shock in our 2D geometry, including spatial non-uniformities and time-dependence, is not a tractable analytic problem and requires 2D simulations beyond the scope of this paper. However, we can still compare our postulated morphology transition with δ_{max} from the 1D theory. As shown in Fig. 5(b), our observed Z_i falls below (and hence δ rises above) the transition threshold (predicted by the 1D theory) around $33 \mu\text{s}$, consistent with the approximate time of the possible morphology transition between Figs. 4(b) and 4(c). While it is far from conclusive that our observations show a shock transition

or a detached shock, they are suggestive and motivate more detailed future work.

IV. OBSERVATION OF MERGED-JET DENSITIES EXCEEDING THAT OF INTERPENETRATION

If the merged-jet emission layers are post-shocked plasma, then we expect an increase in density across the shock boundary during jet merging. The density increase across a 1D shock boundary should satisfy the 1D Rankine-Hugoniot relation¹¹

$$\frac{n_2}{n_1} = \frac{(M_1 \sin \beta)^2 (\gamma + 1)}{(M_1 \sin \beta)^2 (\gamma - 1) + 2}, \quad (2)$$

where n_1 and n_2 are the pre- and post-shock densities, respectively. We bound the theoretically predicted density changes in the system by using $M_1 = 12$ –19, as well as the β range corresponding to the observed $Z_i(\delta)$. We use the conservative value of $\gamma = 1.4$, as suggested by recent work in a similar parameter regime,¹² as a simple way to model ionization and EOS effects in the theoretical estimates of Mach number and density enhancement. Because the Z_i range encompasses $\delta > \delta_{\max}$, we consider the limiting case of detached shock formation (corresponding to a normal shock, i.e., $\beta = 90^\circ$, in 1D theory) in addition to oblique shocks. For an oblique shock with $M = 12$, Eq. (1) gives $\beta = 34^\circ$ – 59° for measured $Z_i = 45$ –25 cm. Thus, the range of $n_2/n_1 = 5.4$ –5.7. Similarly, for $M = 19$ we find $\beta = 34^\circ$ – 58° and $n_2/n_1 = 5.7$ –5.9. Assuming normal shocks ($\beta = 90^\circ$) for $Z_i < 25$ cm, we find $n_2/n_1 = 5.8$ –5.9 for $M = 12$ –19. Thus, the overall range across the shock boundary is $n_2/n_1 = 5.4$ –5.9, according to hydrodynamic 1D theory.

Next we compare n_2/n_1 from the 1D theory with the measured density enhancement $n_{\text{merged}}/n_{\text{single}}$ of the merged- over single-jet cases. We calculate the ion-plus-neutral density n_{tot} using an interferometer phase shift analysis accounting for multiple ionization states and the presence of impurities (see Appendix). According to Eq. (A4), to determine n_{tot} we need the interferometer phase shift $\Delta\phi$, mean charge \bar{Z} , the correction Err [Eq. (A5)] accounting for all non-free-electron contributions to $\Delta\phi$, and the interferometer chord path length (approximated by the plasma jet diameter). The maximum correction Err_{\max} is the largest scaled sensitivity, $C_{0,k}/C_e$ [Eq. (A9)]. These are for Ar I: 0.08 ($\delta N_n^{STP} = 2.8 \times 10^{-4}$ at $\lambda = 561$ nm, $\rho^{STP} = 1.6$ g/L),^{40,41} for O I: 0.03 ($K_{OI}m_O \approx 4.4 \times 10^{-36}$ cm³ for 5000 K $< T < 10000$ K),⁴² and for Al I: 0.007 ($\delta N_n^{STP} = 6.2 \times 10^{-2}$ at $\lambda = 561$ nm, $\rho^{STP} = 2.7$ g/cm³).^{41,43} Thus, $Err_{\max} = 0.08$ (for Ar I).

First, we determine $\Delta\phi_{\text{single}}$ and $\Delta\phi_{\text{merged}}$ for the single- and merged-jet cases, respectively. The single-jet peak $\Delta\phi_{\text{single}}$, averaged across chords for a single shot, is $\Delta\phi_{\text{single}} \approx 4.0^\circ \pm 0.6^\circ$, where 0.6° is the standard deviation [Fig. 6(a)]. The peak $\Delta\phi_{\text{single}}$ averaged over multiple top-jet-only shots at the $R = 2.25$ cm chord is

$\Delta\phi_{\text{single}} = 4.3^\circ \pm 0.3^\circ$ [Fig. 7(b)], and thus we assume $\Delta\phi_{\text{single}} = 4^\circ$ for evaluating $n_{\text{tot},\text{single}} \equiv n_{\text{single}}$. Merged-jet $\Delta\phi_{\text{merged}}$ traces for a single shot show [Fig. 6(b)] a non-uniform spatial profile with a peak near the mid-plane and peak magnitude $\Delta\phi \approx 14^\circ$. At $R = 2.25$ cm, the peak $\Delta\phi = 14.3 \pm 2.4^\circ$ averaged over multiple shots [Fig. 7(b)]. Thus, we assume $\Delta\phi_{\text{merged}} = 14^\circ$ for evaluating $n_{\text{tot},\text{merged}} \equiv n_{\text{merged}}$.

Before evaluating n_{single} and n_{merged} , we examine $\Delta\psi$ enhancements for merged- over single-jet experiments by considering the quantity

$$\Delta\psi = \Delta\phi_{\text{merged}} - (\Delta\phi_{\text{top}} + \Delta\phi_{\text{bottom}}), \quad (3)$$

where $\Delta\phi_{\text{top}}$ and $\Delta\phi_{\text{bottom}}$ are from top-jet-only and bottom-jet-only shots, respectively. We use $\Delta\phi$ values averaged over multiple shots (Fig. 7) to reduce potential errors introduced by shot-to-shot variations. A $\Delta\psi > 0$ implies a density of the merged-jet beyond that of the sum of single jets and/or an increase in \bar{Z} over that of a single jet. Merged-jet measurements over the data set considered (merged-jet: shots 1117–1196; bottom-jet: shots 1277–1278; top-jet: shots 1265–1267) show that $\Delta\psi > 0$ for $R \leq 5.25$ cm [Fig. 7(a)], implying that simple jet interpenetration cannot account for the observed stagnation layer $\Delta\phi_{\text{merged}}$. For $R \geq 6.75$ cm, $\Delta\psi$ is small because this region is outside the stagnation layer.

Now we evaluate n_{single} and n_{merged} in order to estimate the density enhancement $n_{\text{single}}/n_{\text{merged}}$ at $Z \approx 85$ cm and $R \leq 5.25$ cm. Having determined $\Delta\phi$ and Err_{\max} , we need only \bar{Z} to estimate n_{single} and n_{merged} . The T_e and \bar{Z} are determined by comparing spectral data^{1,2} with non-local-thermodynamic-equilibrium (non-LTE) spectral calculations in the optically thin limit using PrismSPECT.⁴⁴ To mitigate the impact of line-of-sight effects on our spectral analysis, we used the appearance (e.g., Ar II) and absence (e.g., impurity Al III) of spectral lines in the data (typically varying only in intensity) in the time range of interest to determine bounds on peak T_e and \bar{Z} . A single jet (assuming 100% Ar) has a jet diameter ≈ 22 cm at $Z \approx 80$ cm and $\bar{Z} = 0.94$ ($T_e = 1.4$ eV) at $Z \approx 41$ cm (the emission is too low at $Z = 85$ cm to infer \bar{Z} there).² Using $\bar{Z} = 0.94$ with $\Delta\phi_{\text{single}} = 4.0^\circ$, we obtain $n_{\text{single}} = 2.1$ – 2.3×10^{14} cm⁻³ (bounds provided by $Err = 0$ and $Err_{\max} = 0.08$). For the 30%/70% mixture case (at the same $T_e = 1.4$ eV), $\bar{Z} = 0.92$,¹ and therefore the n_{single} estimate changes by only a few percent.

To infer \bar{Z} and T_e for the merged-jet case, and therefore n_{merged} , at $Z \approx 85$ cm, we examine spectral data from spectrometer view ‘1.’ For 100% argon, we infer that peak $T_e \geq 1.4$ eV and $\bar{Z} \geq 0.94$.¹ For the 30%/70% mixture, we infer that 2.2 eV \leq peak $T_e < 2.3$ eV and $1.3 \leq \bar{Z} < 1.4$, with the upper bounds determined by the absence of an Al III line in the data.¹ Thus, for the 100% argon case, we see little-to-no change in \bar{Z} compared to the single-jet measurements, but the 30%/70% mixture calculation predicts an increase in \bar{Z} during jet merging, accounting for some of the observed $\Delta\phi$ en-

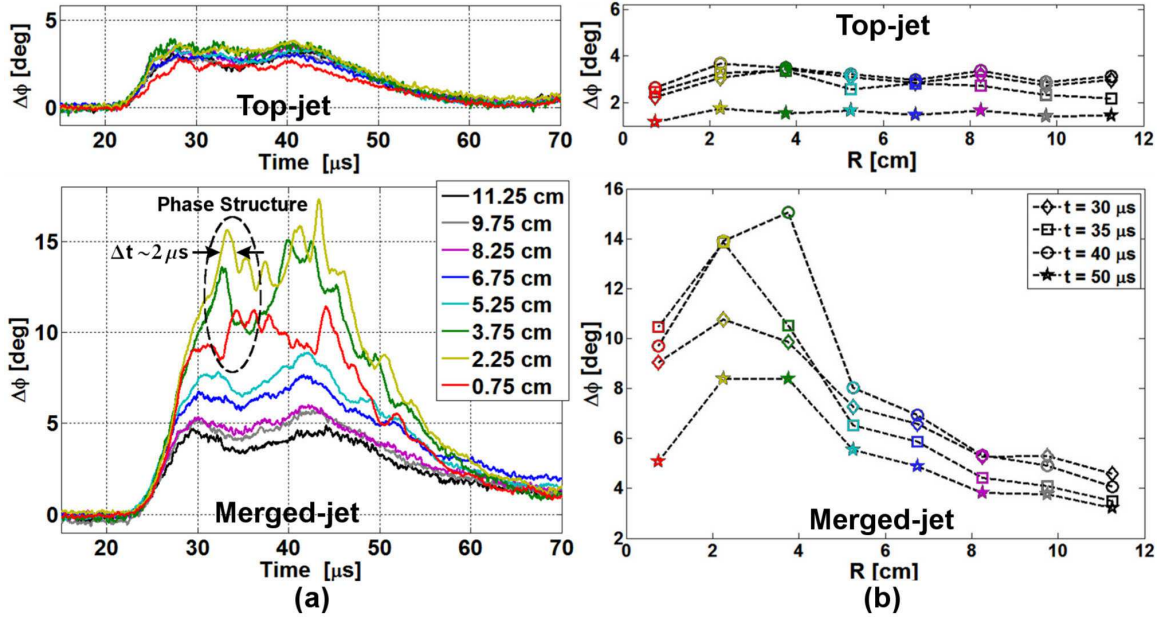


FIG. 6. (a) Phase shift vs. time at $Z \approx 85$ cm for top-jet-only (shot 1265) and merged-jet (shot 1120) cases. The merged-jet phase shift shows multiple small phase peaks of amplitude $\approx 2.5^\circ$ and width $\Delta t \approx 2 \mu$ s. One such phase structure is highlighted by the dashed circle. (b) Phase shift vs. interferometer chord position at several times for the same shots.

hancement. Using $\Delta\phi = 14^\circ$, chord path length of 22 cm, and $\bar{Z} = 0.94$ (100% argon case), we obtain $n_{\text{merged}} = 7.5\text{--}8.2 \times 10^{14} \text{ cm}^{-3}$ (bounds provided by $Err = 0$ and $Err_{\text{max}} = 0.08$). In this case the density increase $n_{\text{merged}}/n_{\text{single}} = 3.2\text{--}3.8$. For the most conservative $\bar{Z} = 1.4$ of the 30%/70% mixture case, $n_{\text{merged}} = 5.0\text{--}5.3 \times 10^{14} \text{ cm}^{-3}$, and $n_{\text{merged}}/n_{\text{single}} = 2.1\text{--}2.4$. These values are summarized in Table I.

The observed range of $n_{\text{merged}}/n_{\text{single}} = 2.1\text{--}3.8$ exceeds the factor of two expected for jet interpenetration, although it is smaller than the $n_2/n_1 = n_{\text{shock}}/n_{\text{unshocked}} = 5.4\text{--}5.9$ predicted by 1D theory. Note that plasma diameter enhancement (along the interferometer chord direction) in the merged- over the single-jet case, which we have not characterized, and overestimates of \bar{Z} (given that we do not have a direct measurement at $Z \approx 85$ cm) would both lead to reductions in our estimate of $n_{\text{merged}}/n_{\text{single}}$. The difference between the measured and predicted density jumps could be due to 3D (e.g., pressure-relief in the out-of-page dimension) and/or plasma EOS effects not modeled by 1D hydrodynamic theory.

We point out a few additional features from the interferometry. The spatial profile for the merged-jet $\Delta\phi$, as seen in Fig. 6(b), is peaked a few centimeters away from the midplane ($R = 0$) and correlates with the peaked emission profile in the R direction, as seen in the CCD images (Fig. 2). Figure 6(a) shows evidence of variations in $\Delta\phi_{\text{peak}} \approx 2.5^\circ$ over $\Delta t \approx 2 \mu$ s in the merged-jet measurements that are not present in single-jet experiments. Assuming $V_{\text{jet}} = 40 \text{ km/s}$, the width of the indi-

cated structure is $\approx 8 \text{ cm}$. The appearance of this $\Delta\phi$ structure alternates between adjacent chords for chords at $R = 0.75\text{--}3.75 \text{ cm}$, i.e., the $\Delta\phi$ rise in one chord corresponds to a fall in another chord at $\approx 1.5 \mu$ s intervals. Because the inter-chord distance is 1.5 cm, the structure has a transverse velocity $\approx 15 \text{ km/s}$. The underlying cause of these structures has not yet been determined.

Electron density results (determined via Stark broadening of the H- β line) at spectrometer view ‘2’ ($Z \approx 55 \text{ cm}$) also show a density enhancement: from $n_e \leq 8.6 \times 10^{13} \text{ cm}^{-3}$ (shot 1106) for a top-jet-only case to $n_e \approx 1.6 \times 10^{15} \text{ cm}^{-3}$ (shot 1101) during jet merging (Fig. 8). The electron density was determined via²

$$n_e = 6.05 \times 10^{14} [\text{FWHM}(\text{pixels})]^{3/2} \text{ cm}^{-3}, \quad (4)$$

	100% Ar	30%/70%
$T_{e,\text{merged}}$	$\geq 1.4 \text{ eV}$	$2.2 \text{ eV} \leq T_e < 2.3 \text{ eV}$
\bar{Z}_{single}	0.94	0.92
\bar{Z}_{merged}	0.94	1.4
n_{single}	$2.1\text{--}2.3 \times 10^{14} \text{ cm}^{-3}$	$2.2\text{--}2.4 \times 10^{14} \text{ cm}^{-3}$
n_{merged}	$7.5\text{--}8.2 \times 10^{14} \text{ cm}^{-3}$	$5.0\text{--}5.3 \times 10^{14} \text{ cm}^{-3}$
$n_{\text{single}}/n_{\text{merged}}$	3.2–3.8	2.1–2.4

TABLE I. Summary of the experimentally inferred jet density enhancement at $Z \approx 85 \text{ cm}$ for the two mixture cases: 100% Ar and 30% Ar/70% impurities. Single-jet and merged-jet densities are calculated using $\Delta\phi = 4^\circ$ and $\Delta\phi = 14^\circ$, respectively, jet diameter of 22 cm, and $Err_{\text{max}} = 0.08$. Note that values for \bar{Z}_{single} are from $Z \approx 41 \text{ cm}$.²

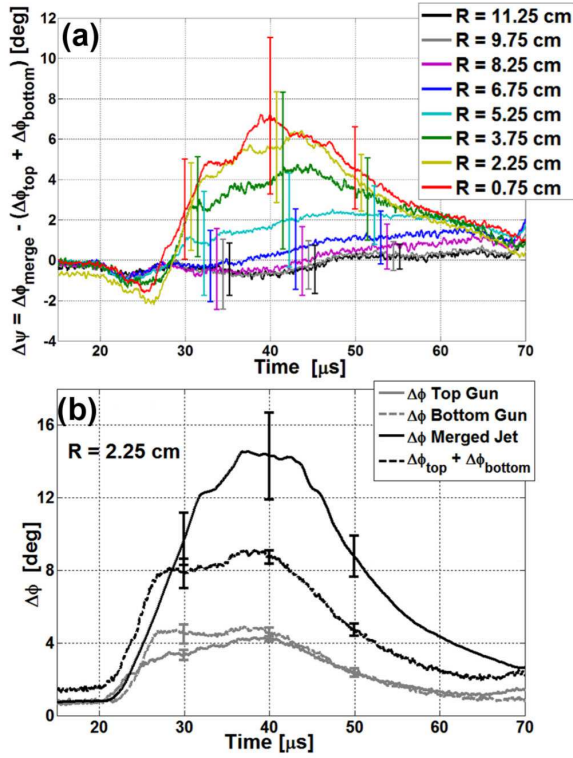


FIG. 7. (a) The difference between merged-jet and the sum of single-jet phase shifts $\Delta\psi$ vs. time for data averaged over shots 1117–1196 (merged-jet), shots 1277–1278 (bottom-jet) and shots 1265–1267 (top-jet). (b) Multi-shot (same data sets) averaged interferometer phase shift vs. time at $R = 2.25$ cm, for top-, bottom-, and merged-jet cases. Error bars indicate the standard deviation of $\Delta\psi$ or $\Delta\phi$ over the stated data set.

where FWHM is the full-width-half-maximum of the Stark-broadened H- β line (more details given in the caption for Fig. 8). For the top-jet-only shot (1106), the FWHM of the Lorentzian (with instrumental broadening removed) is 0.27 pixels, which is significantly less than the 1 pixel spectrometer resolution. So, we consider $n_e = 8.6 \times 10^{13} \text{ cm}^{-3}$ an upper bound, i.e., the density could be less but is too small to be resolvable. Thus, $n_{e,\text{merged}}/n_{e,\text{single}} \gtrsim 10$ at $Z \approx 55$ cm, which is significantly larger than the $n_{\text{merged}}/n_{\text{single}}$ observed at $Z \approx 85$ cm. Some of the $n_e = \bar{Z}n_{\text{tot}}$ increase is likely due to increased ionization during jet merging, but unfortunately there was not enough information in the measured spectrum at $Z \approx 55$ cm to infer \bar{Z} . The $Z \approx 55$ cm measurements were taken at a larger distance from the jet axes than the $Z \approx 85$ cm measurements, which, along with possibly a different \bar{Z} at $Z \approx 55$ cm, could contribute to the difference in density enhancements observed at the two different locations. Nevertheless, the magnitude of the n_e enhancement suggests the presence of post-shocked density also at $Z \approx 55$ cm.

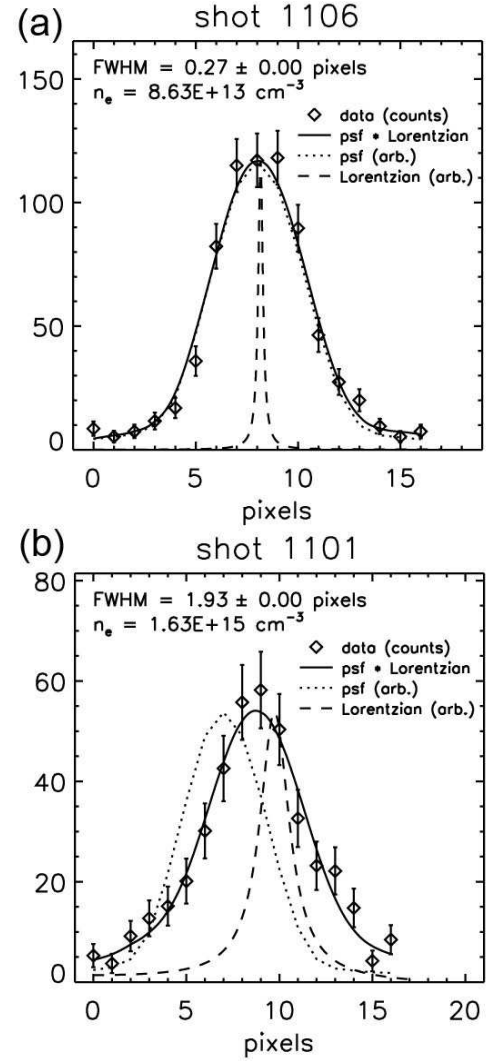


FIG. 8. Determination of electron density n_e at $t = 30 \mu\text{s}$ via Stark broadening of the H- β lines for (a) top-jet-only (shot 1106) and (b) merged-jet (shot 1101) cases at the spectrometer position ‘2’ [see Fig. 1(b)]. Shown are the experimental data (diamonds with error bars $\pm\sqrt{\text{counts}}$), an overlay of the measured instrumental broadening profile (dotted line, labeled as ‘psf’ for point spread function), and a Lorentzian H- β profile (dashed line) that gives the best fit (minimum χ^2) of the convolution (solid line) of the psf and the Lorentzian to the data.

V. COLLISIONALITY ESTIMATES AND COMPARISON TO TWO-FLUID PLASMA SHOCK THEORY

Both the experimentally measured emission¹ and interferometer $\Delta\phi$ [Fig. 6(b)] have the same gradient length scale (few cm) in the R direction, and the $\Delta\phi$ dip at $R = 0.75$ cm and peak at $R = 2.24$ – 3.75 cm [Fig. 6(b)] are well-aligned with the emission dip and peak, respectively.¹ In this section, we compare these observations with the expected scale size of a collisional

plasma shock. In the case of colliding plasmas, the shock scale length is expected³⁴ to be on the order of the ion penetration length into the opposing jet. After evaluating both transverse diffusion and slowing down frequencies,⁴⁵ we find that, in our parameter regime, the limiting physics for ion penetration is frictional drag exerted by the ions of one jet on the counter-streaming ions of the other jet. This is evaluated using the slowing-down rate in the fast approximation,⁴⁵

$$\nu_{ii'}^s = 9.0 \times 10^{-8} n_i' Z^2 Z'^2 \ln \Lambda \left(\frac{1}{\mu} + \frac{1}{\mu'} \right) \frac{\mu^{1/2}}{\epsilon^{3/2}}, \quad (5)$$

where

$$\ln \Lambda = 23 - \ln \left[\frac{Z Z' (\mu + \mu')}{\mu T_{i'} + \mu' T_i} \left(\frac{n_i Z^2}{T_i} + \frac{n_{i'} Z'^2}{T_{i'}} \right)^{1/2} \right] \quad (6)$$

is the Coulomb logarithm for mixed ion-ion collisions,⁴⁵ n_i [cm⁻³] the ion density, Z the charge state, T [eV] the temperature, ϵ [eV] the kinetic energy of the streaming test particle, and the unprimed and primed variables correspond to a test particle from one jet and the field particles of the other jet, respectively. The ion penetration length is

$$\lambda_{ii'}^s \approx v_{\text{rel}} / 4 \nu_{ii'}^s, \quad (7)$$

where v_{rel} is the relative transverse velocity between obliquely merging jets, and the factor of 4 results from the integral effect of v_{rel} slowing down to zero.¹⁴ We estimate $\lambda_{ii'}^s$ by considering jets of 100% argon and the 30%/70% mixture (specifically, 30% Ar, 43% O, 24% Al), in all cases using $v_{\text{rel}} = 20$ km/s (corresponding to $\delta = 30^\circ$ and $Z_i \approx 40$ cm) and the plasma parameters listed in Table II, which also contains a summary of the various length estimates (ion-electron slowing-down distance λ_{ie}^s , using the slow approximation for ν_{ie}^s ,⁴⁵ is also included for comparison). For inter-species collisions in a mixed-species jet (due to impurities), we use $n_i = (\% \text{ ion species}) \times n_{\text{tot}}$.

We also estimate the inter-jet mean free path (mfp) of Ar¹⁺-Ar charge and momentum transfer. The assumption of $v_{\text{rel}} = 20$ km/s gives a kinetic energy of ≈ 80 eV, corresponding to charge and momentum transfer cross-sections $\sigma_{CT} \approx 0.3 \times 10^{-18}$ m² and $\sigma_m \approx 0.7 \times 10^{-18}$ m², respectively.⁴⁶ The total mfp for Ar¹⁺-Ar interaction is $\lambda_{in} = 1/\sigma_{\text{tot}} n_n = 1/[(\sigma_{CT} + \sigma_m) n_n]$, where $n_n = (1 - \bar{Z}) n_{\text{tot}}$ (for $\bar{Z} < 1$) is the neutral density. For 100% argon merged-jet parameters, $\lambda_{in} \approx 2$ cm $\sim \lambda_{ii'}^s$. Comparing all these length scale estimates with the observed few-cm-thick stagnation layer implies that our inter-jet merging is in a semi- to fully collisional regime.

Previously, we showed that the transverse (R) dynamics of our oblique jet merging compared favorably with 1D collisional multi-fluid plasma simulations of our experiment.¹ Specifically, reflected shocks in the simulation (propagating in the R direction) gave rise to a double-peaked density profile (at $\pm R$) consistent with

	100% Ar	30%/70%
n_{tot}	8×10^{14} cm ⁻³	5×10^{14} cm ⁻³
T_e	1.4 eV	2.2 eV
\bar{Z} Ar	0.94	1.2
Al		2.0
O		1.0
$\lambda_{ii'}^s$ Ar-Ar	3.47 cm	2.03 cm
Al-Al		0.16 cm
O-O		0.62 cm
Interspecies		0.57–6.18 cm
λ_{ie}^s Ar	19.4 cm	25.6 cm
Al		6.73 cm
O		14.4 cm

TABLE II. Summary of stopping lengths for inter-jet particle interactions, for both the 100% Ar and 30%/70% mixture cases.

our density and emission profile measurements. Here, we consider our experimental observations in the context of two-fluid plasma shock theory.¹⁶ In the case of a high- M , two-fluid shock, differing ion and electron transport results in shock structures on multiple spatial scales.¹⁶ The length scale of ion viscosity and thermal conduction effects is on the order of the collisional mfp of the shocked ions, $\lambda_i = v_{ti}/\nu_i$, where v_{ti} and ν_i are the ion thermal velocity and thermal collision frequency, respectively, while the length scale of electron viscosity and thermal conduction effects is on the order of $\lambda_i \sqrt{m_i/m_e}$.¹⁶ The range of downstream mfp in our system is estimated to be between 6.4×10^{-3} cm (minimum, from the 30%/70% mixture) and 3.2×10^{-2} cm (maximum, from pure argon) based on the merged-jet parameters given in Table I. In order to bound the range of electron shock scale lengths, we use the limiting cases of $\mu = \mu_O = 16$ and $\mu = \mu_{Ar} = 40$, and obtain $\lambda_i \sqrt{m_i/m_e} \approx 1.1$ –8.6 cm, which is of the same order as the gradient scale length of the observed emission¹ and $\Delta\phi$ profiles [Fig. 6(b)]. This suggests that our observations are also consistent with collisional two-fluid plasma shocks in that the observed scales could be large enough to contain an electron-scale pre-shock.

VI. ON THE USE OF MERGING PLASMA JETS FOR FORMING SPHERICALLY IMPLoding PLASMA LINERS

A key motivation for this work was to study two obliquely merging supersonic plasma jets as the “unit physics” process underlying the use of an array of such jets to form spherically imploding plasma liners. The latter is envisioned as a standoff driver for MIF.^{2,3,6,7,47,48} The dynamics arising in the jet merging, e.g., shock formation, sets the properties of the subsequent, merged plasma that ultimately determines the liner uniformity and peak ram pressure (ρv^2). These physics issues have been considered recently via theory and numeri-

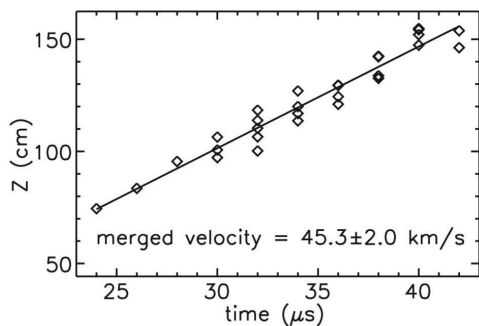


FIG. 9. Leading edge position of the merged jet, as determined visually from CCD images, versus time (shots 1120–1172). Diamonds are data points, and the black line is a linear fit giving the velocity of the merged-jet leading edge.

cal modeling.^{4,49,50} In spherical plasma liner formation via an array of plasma jets, the initial merging would be among more than two jets, and the detailed merging geometry would depend on the port geometry of the vacuum chamber. In the case of PLX, a quasi-spherical arrangement of 60 plasma guns would result in twelve groups of five jets, with each group arranged in a pentagonal pattern.

A key figure of merit for implosion performance is the jet/liner Mach number M , i.e., a lower M results in faster plasma spreading, density reduction, and lower ram pressure.^{5,12,49,51} A concern is that jet merging would lead to shock formation and heating that would significantly decrease M (compared to its initial value) and, thus, implosion performance. The results reported here are encouraging in that the experimentally inferred increases in T_e [by up to a factor of $(2.3 \text{ eV})/(1.4 \text{ eV}) = 1.64$] and \bar{Z} (by up to a factor of $1.4/0.94 = 1.49$) lead to an increase in $C_s \sim (\bar{Z}T_e)^{1/2}$ of 56% (we caution that more data is needed to establish a more accurate upper bound on T_e in the merged case). We estimate the speed of the leading edge of the merged plasma to be $\approx 45 \text{ km/s}$ (see Fig. 9), which is close to the initial jet speed of $\approx 41 \text{ km/s}$. An unchanged velocity after jet merging would result in a modest 36% reduction in M .

With regard to uniformity, the outstanding questions are how the observed structure in two-jet merging would affect the uniformity of the leading edge of an imploding spherical plasma liner formed by multiple merging jets, and how much non-uniformity would be tolerable for compression of a magnetized plasma target for application to MIF. This problem has been studied recently in two simulation studies,^{4,50} which reached opposing conclusions using two different codes employing very different numerical models and techniques. One study concluded that a series of shocks occurring during plasma liner convergence would degrade the implosion performance,⁵⁰ while the other showed that initial non-uniformities arising from jet merging were largely smeared out by the time of peak compression.⁴ More detailed studies are needed to resolve the discrepancy. We

envision a five-jet experiment on PLX followed by a 30- or 60-jet experiment to study this and other issues.

VII. SUMMARY

We have made spatially resolved measurements, in a semi- to fully collisional regime, of the stagnation layer that forms between two obliquely merging supersonic plasma jets. CCD images show a double-peaked emission profile transverse to the layer, with the central emission dip consistent with a density dip observed in the interferometer data. The stagnation layer thickness is a few cm, which is of the same order as the ion penetration length (in our case determined by frictional drag between counter-streaming ions). The observed stagnation layer emission morphology shortly after jet merging is consistent with hydrodynamic oblique shock theory. The density increase from that of an individual jet to the density of the post-merge stagnation layer is greater than that of interpenetration, even accounting for the higher ionization estimates found for the high-impurity versus pure-argon analysis limits. The measured density increase is low compared to 1D theoretical hydrodynamic predictions, but discrepancies are expected due to multi-dimensional and plasma EOS effects in the experiment. We did not observe a strong rise in T_e or \bar{Z} , which, coupled with little observed change in the jet velocity after merging, is encouraging for proposed plasma liner formation experiments.

ACKNOWLEDGMENTS

Significant portions of this work are from E. C. Merritt's doctoral dissertation. We acknowledge HyperV Technologies Corp. for extensive advice on railgun operation, T. P. Intrator and G. A. Wurden for sharing laboratory and diagnostic hardware, and J. T. Cassibry, J. Loverich, and C. Thoma for useful discussions. This work was supported by the U.S. Dept. of Energy.

Appendix A: Interferometer phase shift analysis

Previous interferometer phase shift analysis³⁷ for this experiment assumed a singly ionized argon plasma, which was adequate for our single-jet experiments.² In these two-jet merging experiments, the observation of higher ionization states and significant impurity percentages required generalization of the phase shift analysis.

For a plasma with multiple gas species and ionization states, we can write $\Delta\phi$ as a superposition of the contributions from the electrons and all possible ionization states for each gas species in the plasma:

$$\Delta\phi_{\text{tot}} = \Delta\phi_e - \sum_{j,k} \Delta\phi_{j,k} \quad (\text{A1})$$

$$= \int C_e n_e dl - \int \sum_{j,k} C_{j,k} n_{j,k} dl, \quad (\text{A2})$$

where C_e is the interferometer sensitivity constant for electrons and $C_{j,k}$ is the sensitivity constant for the j th ionization state ($j = 0$ denotes neutrals) of the k th gas species.

For a species with ionization state j , the electron density due to that species is $n_{e,j} = j n_j$. The total electron density is then $n_e = \sum_{j,k} n_{e,(j,k)} = \sum_{j,k} j n_{j,k}$. The average ionization state of the plasma is then

$$\bar{Z} = \frac{n_e}{n_{\text{tot}}} = \frac{\sum_{j,k} n_{e,(j,k)}}{\sum_{j,k} n_{j,k}} = \frac{\sum_{j,k} j n_{j,k}}{\sum_{j,k} n_{j,k}}, \quad (\text{A3})$$

where $n_{\text{tot}} = \sum_{j,k} n_{j,k}$ is the total ion-plus-neutral density of the plasma. The phase shift equation becomes

$$\begin{aligned} \Delta\phi_{\text{tot}} &= \int \left[C_e \bar{Z} n_{\text{tot}} - \sum_{j,k} C_{j,k} n_{j,k} \right] dl \\ &= \int C_e \left[\bar{Z} - \sum_{j,k} \frac{C_{j,k}}{C_e} \frac{n_{j,k}}{n_{\text{tot}}} \right] n_{\text{tot}} dl \\ &\approx C_e [\bar{Z} - \text{Err}] \int n_{\text{tot}} dl, \end{aligned} \quad (\text{A4})$$

assuming a uniform \bar{Z} along the path length through the plasma, and where

$$\text{Err} = \sum_{j,k} \frac{C_{j,k}}{C_e} \frac{n_{j,k}}{n_{\text{tot}}}. \quad (\text{A5})$$

If all the $C_{j,k}$ and $n_{j,k}$ in the plasma are known, then Err can be calculated exactly. However, this is typically prohibitive due to a lack of complete information for both $C_{j,k}$ and $n_{j,k}$. When Err cannot be calculated exactly, it is useful to determine bounds on Err (and thus n_{tot}). Using Eq. (A4) and $\text{Err} = 0$ (i.e., only electrons present), then the lower bound for n_{tot} is given by

$$\left(\int n_{\text{tot}} dl \right)_{\min} = \frac{\Delta\phi_{\text{tot}}}{C_e \bar{Z}}. \quad (\text{A6})$$

Similarly, if we can determine the maximum $\text{Err} = \text{Err}_{\max}$, then an upper bound on n_{tot} is given by

$$\left(\int n_{\text{tot}} dl \right)_{\max} = \frac{\Delta\phi_{\text{tot}}}{C_e [\bar{Z} - \text{Err}_{\max}]}. \quad (\text{A7})$$

One method for determining Err_{\max} is to determine C_{\max} for all j, k present in the plasma, and then define $\text{Err}_{\max} \equiv C_{\max}/C_e$. Because $C_{\max} \geq C_{j,k}$ for all j, k (by definition), then

$$\text{Err} \leq \frac{C_{\max}}{C_e} \sum_{j,k} \frac{n_{j,k}}{n_{\text{tot}}} = \frac{C_{\max}}{C_e} = \text{Err}_{\max} \quad (\text{A8})$$

is always satisfied. The problem then reduces to finding C_{\max} for the given plasma. The $C_{j,k} = (2\pi K_{j,k} m_k)/\lambda$,

where $K_{j,k}$ is the Slater screening constant, m_k is the mass, and λ is the interferometer laser wavelength. Since K is proportional to the sum of mean square electron orbits for all bound electrons,⁵² then for a given gas species k the largest $K_{j,k}$ occurs for the neutral atom, i.e., $K_{\max} = K_{0,k}$. Thus, $C_{\max} = C_{0,k}$ for whichever gas species k in the plasma has the largest neutral sensitivity constant. The maximum correction factor can be written as

$$\text{Err}_{\max} = \frac{(C_{0,k})_{\max}}{C_e} = \frac{2\pi}{C_e \lambda} (K_{0,k} m_k)_{\max} \quad (\text{A9})$$

or, using $K_{j,k} m_k = (\delta N_n^{STP}/n_n^{STP})_k$,^{37,53}

$$\text{Err}_{\max} = \frac{2\pi}{C_e \lambda} \left(\frac{N_n^{STP}}{n_n^{STP}} \right)_{k,\max}, \quad (\text{A10})$$

where n_n^{STP} is the neutral density of the species at standard temperature and pressure, N_n is the refractive index of the neutral species, $\delta N_n = N_n - 1$, and $C_e = \lambda e^2 / (4\pi\epsilon_0 m_e c^2)$.

- ¹E. C. Merritt, A. L. Moser, S. C. Hsu, J. Loverich, and M. A. Gilmore, Phys. Rev. Lett. **111**, 085003 (2013).
- ²S. C. Hsu, E. C. Merritt, A. L. Moser, T. J. Awe, S. J. E. Brockington, J. S. Davis, C. S. Adams, A. Case, J. T. Cassibry, J. P. Dunn, M. A. Gilmore, A. G. Lynn, S. J. Messer, and F. D. Witherspoon, Phys. Plasmas **19**, 123514 (2012).
- ³S. C. Hsu, T. J. Awe, S. Brockington, A. Case, J. T. Cassibry, G. Kagan, S. J. Messer, M. Stanic, X. Tang, D. R. Welch, and F. D. Witherspoon, IEEE Trans. Plasma Sci. **40**, 1287 (2012).
- ⁴J. T. Cassibry, M. Stanic, S. C. Hsu, F. D. Witherspoon, and S. I. Abarzhi, Phys. Plasmas **19**, 052702 (2012).
- ⁵J. T. Cassibry, M. Stanic, and S. C. Hsu, Phys. Plasmas **20**, 032706 (2013).
- ⁶Y. C. F. Thio, E. Panarella, R. C. Kirkpatrick, C. E. Knapp, F. Wysocki, P. Parks, and G. Schmidt, in *Current Trends in International Fusion Research—Proceedings of the Second International Symposium*, edited by E. Panarella (NRC Canada, Ottawa, 1999) p. 113.
- ⁷Y. C. F. Thio, C. E. Knapp, R. C. Kirkpatrick, R. E. Siemon, and P. J. Turchi, J. Fusion Energy **20**, 1 (2001).
- ⁸I. R. Lindemuth and R. C. Kirkpatrick, Nucl. Fusion **23**, 263 (1983).
- ⁹R. C. Kirkpatrick, I. R. Lindemuth, and M. S. Ward, Fusion Tech. **27**, 201 (1995).
- ¹⁰I. R. Lindemuth and R. E. Siemon, Amer. J. Phys. **77**, 407 (2009).
- ¹¹R. P. Drake, *High-Energy-Density-Physics* (Springer, Berlin, 2006).
- ¹²T. J. Awe, C. S. Adams, J. S. Davis, D. S. Hanna, S. C. Hsu, and J. T. Cassibry, Phys. Plasmas **18**, 072705 (2011).
- ¹³A. Case, S. Messer, S. Brockington, L. Wu, F. D. Witherspoon, and R. Elton, Phys. Plasmas **20**, 012704 (2013).
- ¹⁴S. Messer, A. Case, L. Wu, S. Brockington, and F. D. Witherspoon, Phys. Plasmas **20**, 032306 (2013).
- ¹⁵W. Linchun, M. Phillips, S. Messer, A. Case, and F. D. Witherspoon, IEEE Trans. Plasma Sci. **41**, 1011 (2013).
- ¹⁶M. Y. Jaffrin and R. F. Probst, Phys. Fluids **7**, 1658 (1964).
- ¹⁷R. A. Bosch, R. L. Berger, B. H. Failor, N. D. Delamater, G. Charatis, and R. L. Kauffman, Phys. Fluids B **4**, 979 (1992).
- ¹⁸O. Rancu, P. Renaudin, C. Chenais-Popovics, H. Kawagashi, J. C. Gauthier, M. Dirksmoller, T. Missalla, I. Uschmann, E. Forster, O. Larroche, O. Peyrusse, O. Renner, E. Krousky, H. Pepin, and T. Shepard, Phys. Rev. Lett. **75**, 3854 (1995).
- ¹⁹A. S. Wan, T. W. Barbee, Jr., R. Cauble, P. Celliers, L. B. Da Silva, J. C. Moreno, P. W. Rambo, G. F. Stone, J. E. Trebes, and F. Weber, Phys. Rev. E **55**, 6293 (1997).

- ²⁰N. C. Woolsey, Y. Abou, R. G. Evans, R. A. D. Grundy, S. J. Pestehe, P. G. Carolan, N. J. Conway, R. O. Dendy, P. Helander, K. G. McClements, J. G. Kirk, P. A. Norreys, M. M. Notley, and S. J. Rose, *Phys. Plasmas* **8** (2001).
- ²¹L. Romagnani, S. V. Bulanov, M. Borghesi, P. Audebert, J. C. Gauthier, K. Lowenbruck, A. J. Mackinnon, P. Patel, G. Pretzler, T. Toncian, and O. Willi, *Phys. Rev. Lett.* **101**, 025004 (2008).
- ²²Y. Kuramitsu, Y. Sakawa, T. Morita, C. D. Gregory, J. N. Waugh, S. Dono, H. Aoki, H. Tanji, M. Koenig, N. Woolsey, and H. Takabe, *Phys. Rev. Lett.* **106**, 175002 (2011).
- ²³N. Kugland, D. D. Ryutov, P.-Y. Chang, R. P. Drake, G. Fiksel, D. H. Froula, S. H. Glenzer, G. Gregori, M. Grosskopf, M. Koenig, Y. Kuramitsu, C. Kuran, M. C. Levy, E. Liang, J. Meinecke, F. Miniati, T. Morita, A. Pelka, C. Plechaty, R. Presura, A. Ravasio, B. A. Remington, B. Reville, J. S. Ross, Y. Sakawa, A. Spitkovsky, H. Takabe, and H.-S. Park, *Nature Phys.* **8**, 809 (2012).
- ²⁴J. S. Ross, S. H. Glenzer, P. Amendt, R. Berger, L. Divol, N. L. Kugland, O. L. Landen, C. Plechaty, B. Remington, D. Ryutov, W. Rozmus, D. H. Froula, G. Fiksel, C. Sorce, Y. Kuramitsu, T. Morita, Y. Sakawa, H. Takabe, R. P. Drake, M. Grosskopf, C. Kuran, G. Gregori, J. Meinecke, C. D. Murphy, M. Koenig, A. Pelka, A. Ravasio, T. Vinci, E. Liang, R. Presura, A. Spitkovsky, F. Miniati, and H.-S. Park, *Phys. Plasmas* **19**, 056501 (2012).
- ²⁵G. F. Swadling, S. V. Lebedev, N. Niasse, J. P. Chittenden, G. N. Hall, F. Suzuki-Vidal, G. Burdiak, A. J. Harvey-Thompson, S. N. Bland, P. De Grouchy, E. Khoory, L. Pickworth, J. Skidmore, and L. Suttle, *Phys. Plasmas* **20**, 022705 (2013).
- ²⁶G. F. Swadling, S. V. Lebedev, G. N. Hall, F. Suzuki-Vidal, G. Burdiak, A. J. Harvey-Thompson, S. N. Bland, P. De Grouchy, E. Khoory, L. Pickworth, J. Skidmore, and L. Suttle, *Phys. Plasmas* **20**, 062706 (2013).
- ²⁷H. Luna, K. D. Kavanagh, and J. T. Costello, *J. Appl. Phys.* **101**, 033302 (2007).
- ²⁸C. Sánchez-Aké, D. Mustri-Trejo, T. García-Fernández, and M. Villagrán-Muniz, *Spectrochimica Acta B* **65**, 401 (2010).
- ²⁹P. Hough, C. McLoughlin, T. J. Kelly, P. Hayden, S. S. Harilal, J. P. Mosnier, and J. T. Costello, *J. Phys. D: Appl. Phys.* **42**, 055211 (2009).
- ³⁰P. Hough, C. McLoughlin, S. S. Harilal, J. P. Mosnier, and J. T. Costello, *J. Appl. Phys.* **107**, 024904 (2010).
- ³¹P. Yeates, C. Fallon, E. T. Kennedy, and J. T. Costello, *Phys. Plasmas* **18** (2011).
- ³²R. L. Berger, J. R. Albritton, C. J. Randall, E. A. Williams, W. L. Kruer, A. B. Langdon, and C. J. Hanna, *Phys. Fluids B* **3**, 3 (1991).
- ³³S. M. Pollaine, R. L. Berger, and C. J. Keane, *Phys. Fluids B* **4**, 989 (1992).
- ³⁴P. W. Rambo and J. Denavit, *Phys. Plasmas* **1**, 4050 (1994).
- ³⁵P. W. Rambo and R. J. Procassini, *Phys. Plasmas* **2**, 3130 (1995).
- ³⁶E. C. Merritt, A. G. Lynn, M. A. Gilmore, and S. C. Hsu, *Rev. Sci. Instrum.* **83**, 033506 (2012).
- ³⁷E. C. Merritt, A. G. Lynn, M. A. Gilmore, C. Thoma, J. Loverich, and S. C. Hsu, *Rev. Sci. Instrum.* **83**, 10D523 (2012).
- ³⁸L. D. Landau and E. M. Lifshitz, *Fluid Mechanics 2nd Ed.* (Butterworth-Heinemann, 2011) pp. 313–350.
- ³⁹R. H. Nunn, *Intermediate Fluid Dynamics* (Hemisphere Publishing, New York, 1989) pp. 128–134.
- ⁴⁰M. J. Weber, *Handbook of Optical Materials*, 1st ed. (CRC Press, Boca Raton, 2003) pp. 447–449.
- ⁴¹D. R. Lide, *Handbook of Chemistry and Physics*, 83rd ed. (CRC Press, Boca Raton, 2002–2003) pp. 4–39–4–96.
- ⁴²A. V. Ivanova and V. N. Kologrivov, *J. Appl. Spect.* **13**, 961 (1970).
- ⁴³A. D. Rakić, *Appl. Optics* **34**, 4755 (1995).
- ⁴⁴J. J. MacFarlane, I. E. Golovkin, P. R. Woodruff, D. R. Welch, B. V. Oliver, T. A. Mehlhorn, and R. B. Campbell, in *Inertial Fusion Sciences and Applications 2003*, edited by B. A. Hammel, D. D. Meyerhofer, and J. Meyer-ter-Vehn (American Nuclear Society, La Grange Park, IL, 2004) p. 457.
- ⁴⁵J. D. Huba, *NRL Plasma Formulary*, 2011.
- ⁴⁶A. V. Phelps, *J. Phys. Chem. Ref. Data* **20**, 557 (1990).
- ⁴⁷J. T. Cassibry, R. J. Cortez, S. C. Hsu, and F. D. Witherspoon, *Phys. Plasmas* **16**, 112707 (2009).
- ⁴⁸J. F. Santarius, *Phys. Plasmas* **19**, 072705 (2012).
- ⁴⁹P. B. Parks, *Phys. Plasmas* **15**, 062506 (2008).
- ⁵⁰H. Kim, L. Zhang, R. Samulyak, and P. Parks, *Phys. Plasmas* **20**, 022704 (2013).
- ⁵¹J. S. Davis, S. C. Hsu, I. E. Golovkin, J. J. MacFarlane, and J. T. Cassibry, *Phys. Plasmas* **19**, 102701 (2012).
- ⁵²R. A. Alpher and D. R. White, *Phys. Fluids* **2**, 153 (1959).
- ⁵³D. Kumar, *Experimental Investigations of Magnetohydrodynamic Plasma Jets*, Ph.D. thesis, California Institute of Technology (2009).